Thin–Walled Structures 204 (2024) 112280

Contents lists available at ScienceDirect

Thin-Walled Structures

journal homepage: www.elsevier.com/locate/tws

Full length article

Controlled swelling-induced shape change of soft gel filled structures

Silvia Monchetti [a], Roberto Brighenti [a,*], Tamara Hanuhov [b], Noy Cohen [b]

[a] Department of Civil and Environmental Engineering, University of Florence, Via di S. Marta 3 - 50139 Firenze, Italy
[b] Department of Materials Science and Engineering, Technion - Israel Institute of Technology, Haifa 3200003, Israel

ARTICLE INFO

Keywords:
Gels
Confined swelling
Volume expansion
Controlled shape change
Machine learning
Inverse problem

ABSTRACT

Gels are polymers that can imbibe large amounts of solvent and generate large volumetric deformations in a process commonly termed swelling. The swelling-induced deformations can be harnessed to produce pressure against surrounding elastic elements, and therefore lead to spatial shape changes without the need for an external energy source. In the present paper, we consider a thin cylindrical elastic tube that encapsulates a gel and deforms in response to the swelling-induced forces. It is expected that by controlling the spatial stiffness distribution of the tube, the deformed swelling-induced shape can be programmed. We exploit this simple idea to obtain controlled shape change driven by the large volumetric expansion of gels. To this end, we train a machine learning algorithm through many FE simulations that enable solving the inverse problem: for any prescribed swelling-induced target shape, the algorithm provides the spatial stiffness distribution of the thin tube. The results confirm that precise controlled shape change is achievable by exploiting the large swelling-induced volumetric deformations in an autonomous manner (i.e. without the need for any external energy source). This work paves the way for new perspectives in the design of shape-change systems based on the simple yet proper elastic distribution of confining structures.

1. Introduction

Gels comprise a polymer network that imbibes a large amount of solvent and experiences large volumetric deformations. A particular class of gels is represented by hydrogels, polymers with a high affinity for water. Thanks to their ease of synthesis, low cost, biocompatibility, and ability to experience large deformations, hydrogels are employed in many advanced applications such as drug delivery, agriculture, tissue engineering, and biosensors [1–4].

In recent applications, gels swelling under mechanical [5,6], chemo-mechanical [7,8], or bio-mechanical constraints [9] have been considered; moreover, temperature-sensitive gels enable controlling their swelling degree through suitable external stimuli [10]. As a result, gels interact with other components in the system and exert forces on them [11–16]; this mechanism can be harnessed to produce energy by coupling gels with dielectric elastomers [17] or with piezoelectric polymers, or to induce deformation in multilayer structures [18]. These interactions can lead to complex deformations [19–21] and can be advantageous. For example, swelling-induced shape changes in hydrogels are exploited in drug delivery to release active substances in response to stimuli such as pH at target sites. This enables precise spatio-temporal control over drug delivery [22]. Biosensors are another example of a device that responds to swelling-induced forces to detect changes in the surrounding environment (such as the presence of specific biomolecules or variations in pH) by providing a measurable physical signal [16,23].

The research on swelling-induced shape changes in gels is rapidly evolving, with new materials and synthesis techniques improving constantly. Current efforts focus on the activation of shape changes in stimuli-responsive materials [24] that can potentially achieve other functionalities such as self-healing or biodegradation through swelling mechanisms [25,26]. Overall, the ability to induce and harness changes in shape due to swelling-induced mechanisms shows promise with the potential to revolutionize various technological and biomedical fields [27].

In this work, we propose to induce changes in shape through swelling-induced forces and the mechanical interactions of gels with passive (non-swelling) components. As an example, consider a cylindrical gel that is placed in a soft elastic ring, as shown in Fig. 1a. The system is placed in an appropriate solvent and the gel begins to swell. Once the gel comes into contact with the elastic layer, it exerts forces that lead to deformations and shape changes in the ring. In the case of a homogeneous confining elastic ring, the tube increases and dilates while maintaining a circular shape (see Fig. 1b). However, if the ring is heterogeneous, i.e. its stiffness distribution varies spatially, the swelling-induced forces lead to a deviation from the circular shape

* Corresponding author.
E-mail addresses: roberto.brighenti@unifi.it (R. Brighenti), noyco@technion.ac.il (N. Cohen).

https://doi.org/10.1016/j.tws.2024.112280
Received 25 May 2024; Received in revised form 22 July 2024; Accepted 27 July 2024
Available online 2 August 2024

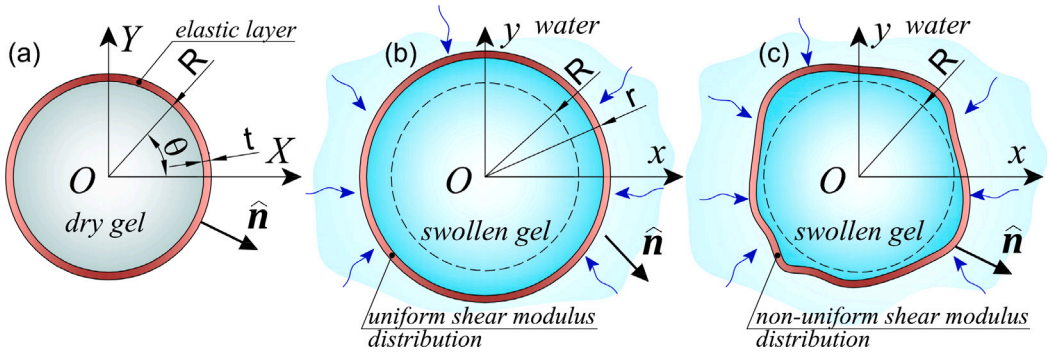

Fig. 1. The swelling of a cylindrical gel in a confining elastic ring: (a) dry gel (reference configuration), (b) deformation due to swelling in a homogeneous elastic ring, (c) deformation due to swelling in a heterogeneous ring with spatially varying stiffness distribution.

(see Fig. 1c). An example in a biological context was recently illustrated in Ref. [28]. By tuning the stiffness distribution of the ring, the deformations of the ring itself can be programmed into a target shape.

The coupling and interactions between the gel and the elastic layer pose numerical difficulties. With the aim of deriving a design guide that enables us to prescribe a target shape and obtain the spatial stiffness distribution of the elastic ring, we employ machine learning (ML) methods. The ML algorithm is trained with finite-element simulations on a variety of stiffness distributions. We follow by exploiting the ML algorithm to determine the stiffness distribution along the elastic ring required to achieve a variety of complex planar configurations in response to swelling-induced forces.

2. Swelling of gels under constraints

Consider a polymer network occupying a volume B_0 with a boundary ∂B_0. The material points in the dry polymer are denoted by $\mathbf{X}$. The network is placed in a cylindrical ring, which is filled with an appropriate solvent. Due to the diffusion of solvent molecules into the network, the gel swells. In the deformed swollen configuration, the gel occupies a volume B with a boundary ∂B. The material points are denoted by $\mathbf{x}$. The deformation gradient from the reference to the deformed swollen configuration is $\mathbf{F} = \partial\mathbf{x}/\partial\mathbf{X}$ and the volumetric deformations are $J = \det\mathbf{F} = 1 + C_s v_s$, where C_s is the uptake concentration and v_s is the molar volume of the solvent.

To determine the equilibrium response, we follow common practice [29–32], which couples the elasticity of the tube to the swelling of the filling gel, and assume that the elastic response of the gel can be determined from an energy-density function written as follows:

$$\Psi = (\Psi_{net} + \Psi_{mix}) + \pi(1 + v_s C_s - J) \tag{1}$$

where Ψ_{net} is the energy density due to the deformation of the network, Ψ_{mix} is the mixing energy density, and π is a workless pressure-like term that enforces the volumetric constraints and is determined from the boundary conditions.

In this work, we consider Neo-Hookean materials characterized by a deformation energy-density function

$$\Psi_{net} = \frac{\mu}{2}\left(I_1 - 3\right), \tag{2}$$

where $I_1 = \mathrm{tr}\left(\mathbf{F}\mathbf{F}^T\right)$ is the first invariant and μ is the shear modulus. The mixing term derived in the works of Huggins [33] and Flory [34] reads

$$\Psi_{mix} = \frac{k_B T}{v_s}\left[(J-1)\ln\frac{v_s C_s}{J} + v_s C_s \frac{\chi}{J}\right], \tag{3}$$

where k_B is the Boltzmann constant, T is the temperature, and χ is a dimensionless interaction parameter governing the gel-solvent affinity.

2.1. Numerical simulation of swelling

The swelling problem is highly non-linear and only a few specific cases can be solved analytically [11]. In other cases, numerical and computational approaches are required, typically implemented within a finite element-based framework. To this end, we employ the variational formulation and phrase it in a discretized form.

The stationarity of the energy of the system, evaluated over the reference domain B_0 with boundary $\partial B_0 = \partial B_u \cup \partial B_t$ (where ∂B_u and ∂B_t the portions of the boundary where the displacements $\boldsymbol{u}$ and the tractions $\boldsymbol{T}$ are prescribed, respectively), requires the following variation to be zero

$$\delta\Pi = \int_{B_0} \delta\Psi dv - \int_{B_0} \boldsymbol{B}\cdot\delta\boldsymbol{u} dV - \int_{\partial B_t} \boldsymbol{T}\cdot\delta\boldsymbol{u} dS = 0, \tag{4}$$

where $\boldsymbol{B}$ denotes body forces, and $\delta\bullet$ indicates a generic variation of the quantity $\bullet$.

In the case of isothermal conditions, the above variation has to be assessed with respect to the displacement gradient and the solvent concentration, i.e. $\nabla\mathbf{u}$ and C_s. Specifically,

$$\begin{aligned}\delta_{\boldsymbol{u},C_s}\Pi = &\int_{B_0} \frac{\partial(\Psi_{net}(\boldsymbol{F}) + \Psi_{mix}(C_s) + \pi(1 + v_s C_s - J))}{\partial\nabla\boldsymbol{u}}\delta\nabla\boldsymbol{u} dV \\ &+ \int_{B_0} \frac{\partial(\Psi_{net}(\boldsymbol{F}) + \Psi_{mix}(C_s) + \pi(1 + v_s C_s - J))}{\partial C_s}\delta C_s dV \\ &- \int_{B_0} \boldsymbol{B}\cdot\delta\boldsymbol{u} dV - \int_{\partial B_t} \boldsymbol{T}\cdot\delta\boldsymbol{u} dV = \\ &\int_{B_0} (\boldsymbol{P} + \pi J\boldsymbol{F}^{-T})\delta\boldsymbol{u} dV + \int_{B_0} (\mu_c + \pi v_s)\delta C_s dV - \int_{B_0} \boldsymbol{B}\cdot\delta\boldsymbol{u} dV \\ &- \int_{\partial B_t} \boldsymbol{T}\cdot\delta\boldsymbol{u} dS = 0.\end{aligned} \tag{5}$$

Here, $\boldsymbol{P} = \partial\Psi_{net}/\partial\boldsymbol{F}$ denotes the first Piola–Kirchhoff stress tensor and $\mu_c = \partial\Psi_{mix}/\partial C_s$ indicates the so-called chemical potential.

In general, the problem has to be solved by considering the following mechanical and chemical boundary conditions: $\boldsymbol{u} = \bar{\boldsymbol{u}}$ on ∂B_u, $(\boldsymbol{P} + \pi J\boldsymbol{F}^{-T})\boldsymbol{n} = \bar{\boldsymbol{T}}$ on $\partial\Omega_t$, and $\mu_c = \bar{\mu}_c$ on $\partial\Omega_c$, where $\bar{\bullet}$ indicates a prescribed value of a variable of the problem on the domain boundary and $\partial\Omega_c$ is the portion of the boundary where the chemical potential is assigned, corresponding to the portion of the gel domain in contact with the solvent. In the present study, we impose displacement boundary conditions to some FE nodes of the discretized domain to prevent any possible rigid body motion of the system, and the chemical potential to boundary regions in direct contact with the fluid; no traction forces are assumed to be applied.

To solve numerically the problem of swelling under mechanical constraints, the above-illustrated variational (weak form) of the problem can be straightforwardly implemented within a finite element framework. This requires that the involved variables (namely the displacement field $\boldsymbol{u}$, the chemical potential μ_c, and the osmotic pressure

π), are expressed throughout the domain by using the FE nodal values counterparts indicated with $\hat{\bullet}$ in the following,

$$\begin{aligned}\tilde{\boldsymbol{u}} &= \sum_{i=1}^{n_n}[N]_i\hat{\boldsymbol{u}}_i,\\ \tilde{\mu}_c &= \sum_{i=1}^{n_n}[N]_i\hat{\mu}_{ci},\\ \tilde{\pi} &= \sum_{i=1}^{n_n}[N]_i\hat{\pi}_i,\\ \nabla\cdot\tilde{\boldsymbol{\xi}} = \nabla\cdot\sum_{i=1}^{n_n}[N]_i\hat{\boldsymbol{\xi}}_i &= \sum_{i=1}^{n_n}[B]_i\hat{\boldsymbol{\xi}}_i\end{aligned} \tag{6}$$

where $[N]_i$ and $[B]_i$ are the standard finite element shape function and compatibility matrix, respectively, associated with the ith node of the FE discretization, respectively, n_n is the number of nodes of one FE, while $\nabla\cdot\boldsymbol{\xi}$ indicates the divergence operator applied to the generic quantity $\boldsymbol{\xi}$. In Eq. (6), the generic quantity interpolated by using the nodal values has been indicated with $\tilde{\bullet}$.

Discretizing the variational form (5) by using the involved quantities expressed through the corresponding nodal values expressed by Eq. (6), leads to the following force and flux balance conditions [35]

$$\begin{aligned}\boldsymbol{R}^e_u &= \int_{B_{0e}}[B]^T(\boldsymbol{P}+\pi J\boldsymbol{F}^{-T})dV - \int_{B_{0e}}[N]^T\boldsymbol{B}dV - \int_{\partial B_{te}}[N]^T\boldsymbol{T}\ dS = \boldsymbol{0}\\ \boldsymbol{R}^e_{\mu_c} &= \int_{B_{0e}}J^{-1}\frac{C_sD}{k'_BT}[B]^T[B]dV\{\hat{\mu_c}\} + \int_{B_{0e}}J^{-1}\frac{\partial C_s}{\partial\mu_c}[N]^T[N]dV\{\dot{\hat{\mu_c}}\}+\\ &\quad+\int_{B_{0e}}J^{-1}\frac{\partial C_s}{\partial\pi}[B]^T[B]dV\{\dot{\hat{\pi}}\} + \int_{\partial B_{\mu_c}}[N]^T\boldsymbol{j}_n\ dS = \boldsymbol{0}\end{aligned} \tag{7}$$

that for simplicity have been written by referring to the single finite element e in the undeformed configuration whose domain is B_{0e}; the last integral of Eq. ($(7)_2$) accounts for the fluid flux occurring on the portion ∂B_{μ_c} of the boundary where the chemical potential is known, with $\boldsymbol{j}_n = -\frac{C_sD}{k'_BT}\nabla\mu_c$ [36], $k'_B = k_BA_n$, A_n the Avogadro's number, D the diffusion coefficient of the gel, while the superscript $\bullet^T$ indicates the transpose operator, and $\dot{\bullet}$ the time derivative. The solution of the non-linear multi-physics above-stated problem requires the two vectors in (7) to vanish for the involved balance equations to be fulfilled. The two above residuals are made to converge to zero with a given small tolerance value, through a standard iterative process leading to the displacements and chemical potential fields in the domain of interest.

Problems involving coupling of various physics, such as the fluid diffusion and the network mechanics, can be solved numerically in a staggered or monolithic way; the first approach is simpler and, if the time step adopted is sufficiently small, the solution is relatively accurate. It is based on the concept of freezing the fluid diffusion problem during a small time step while the mechanical problem is solved, and by assuming the previously converged mechanical configuration of the system to be fixed, while the diffusion problem is advanced further in the time domain. The staggered approach is adopted in the present computational framework.

3. Machine learning-based control of shape change

Programming the swelling-induced shape changes of an elastic tubular structure in response to the swelling of a gel requires the tuning of the spatial shear modulus distribution within the elastic layer. This is typically termed the inverse problem. Once such solutions are obtained, an elastic tube with the appropriate properties can be fabricated (typically via additive manufacturing technologies).

The computation of the deformed swelling-induced shape of a tube involves a highly non-linear and complex set of equations. Fig. 2 highlights this through the illustration of three spatial stiffness distributions in an elastic ring and the corresponding swelling-induced deformations. As shown, stiffer regions experience smaller deformations than softer ones along the elastic ring, and the variations in the stiffness along the contour lead to a deviation from the circular cross-section.

In the following, we solve the inverse problem using an Artificial Neural Network (ANN) model [13,37,38]. An ANN is a specific type of Machine Learning (ML) algorithm, inspired by the structure and functionality of the human brain. ANNs have been applied to a variety of problems thanks to their ability to learn complex patterns and relationships [39]. Methods based on Physics-Informed NN (PINNs) have been developed for tackling engineering problems – whose governing differential equations are solved by minimizing the residual of some energy functional – by employing the universal approximation property of ANN to represent the solution field [40,41]. An ANN consists of interconnected nodes (artificial neurons) arranged in layers. Information flows through the network from the input layer to the final output one, undergoing various transformations. In this work, the ANN is trained with several finite element simulations of a gel that swells inside a tubular ring with different stiffness distributions.

The architecture of an ANN, i.e. the number and types of layers it is made of, impacts the learning capacity and performance. In other words, an ANN dynamically adjusts the weights and biases based on data provided to the system through an iterative calculation encompassing: (1) a forward process (input data propagates through the layers, undergoing transformations at each layer based on the activation functions and weights); (2) an error calculation performed by comparing the network output to the desired one; (3) a back-propagation process aimed at adjusting the weights and biases in order to reduce as much as possible the contribution of each weight to the overall error.

3.1. ANN-based shape change inverse design

In general, an ANN operates through several layers which transform the incoming information into the final quantity we want to predict through the ANN itself once properly trained (see Fig. 3). In the following, we define the input vector $x_h = \bar{r}_h$, where $\bar{r}_h$ are the dimensionless radius values with $h = 1,\dots,m$ the number of points used to discretize the external boundary of the elastic layer surrounding the gel. The output vector $y^{(N)}_l = \bar{\mu}^{(N)}_l$ denotes the dimensionless shear modulus at discrete position $l = 1,\dots,p$ along the perimeter of the elastic ring. The flow of data can be described as follows,

$$\begin{aligned}z^{(1)}_j &= w^{(1)}_{jh}x_h + b^{(1)}_1,\\ y^{(1)}_k &= \sigma_1(z^{(1)}_k)\\ z^{(2)}_j &= w^{(2)}_{jk}y^{(1)}_k + b^{(2)}_j = w^{(2)}_{jk}\sigma_1(z^1_k) + b^{(2)}_j,\ (k=1,\dots,q)\\ &\dots\\ z^{(N-1)}_j &= w^{(N-1)}_{jk}\sigma_{N-2}(z^{(N-2)}_k) + b^{(N-1)}_j\\ z^{(N)}_l &= w^{(N)}_{lk}\sigma_{N-1}(z^{(N-1)}_k) + b^{(N)}_l = w^{(N)}_{lk}y^{(N-1)}_k + b^{(N)}_l\\ y^{(N)}_l &= \sigma_N z^{(N)}_l,\end{aligned} \tag{8}$$

where w_{jk} and b_j denote the weight matrix and the bias vector, respectively, used to transform the information coming from layer j to layer $j+1$, and σ is the so-called activation function whose role is to account for the non-linearities of the problem. In Eqs (8) the summation over the repeated indices has been adopted.

The output of the ANN is represented by the vector $\bar{\mu}^{(N)}_l$ containing the dimensionless distribution of the shear modulus values of the surrounding elastic layer. The ANN assumes hidden layers with q neurons each. Layers 0 and N comprise m and p neurons, respectively (see Fig. 3). For the generic hidden layer i, $1 \le i \le N-1$, the transformation of the information flowing through the ANN can be written as

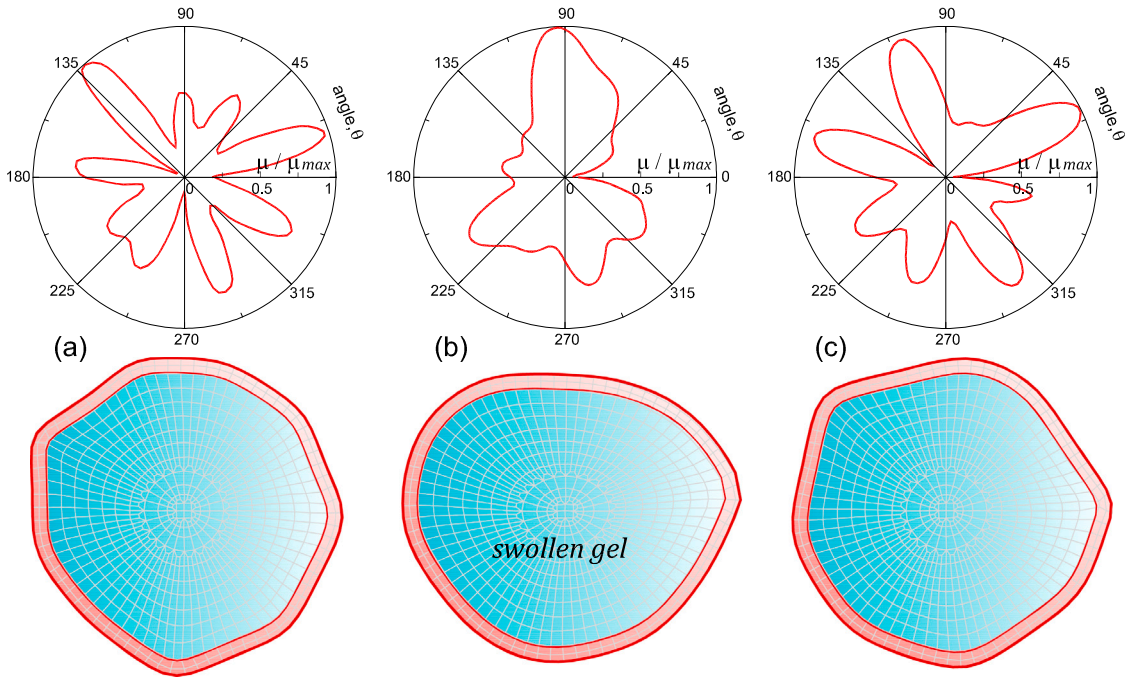

Fig. 2. Examples of the shape change obtained by FEM simulations of the gel-elastic layer (with a randomly distributed shear modulus) system upon swelling. Dimensionless shear modulus distribution (top) and corresponding final shape (down) for three different cases.

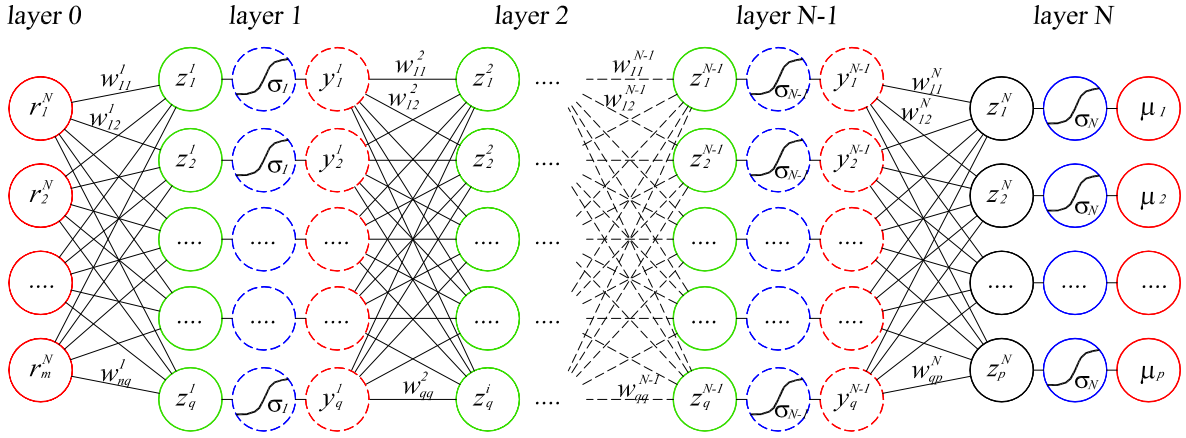

Fig. 3. Schematic of the neural network algorithm trained to determine the final shape of the confined gel sphere enclosed in an elastic layer with a distribution of shear modulus μ_i.

$$\boldsymbol{y}^{(i)} = \boldsymbol{w}^{(i)}\sigma_{i-1}(\boldsymbol{z}^{(i-1)}) + \boldsymbol{b}^{(i)} = \boldsymbol{w}^{(i)}\boldsymbol{y}^{(i-1)} + \boldsymbol{b}^{(i)}. \tag{9}$$

The ANN procedure starts from an initial data $x = [x_1, x_2, \dots, x_m]^T$ and the corresponding known target outputs $y = [y_1, y_2, \dots, y_p]^T$. The aim of the algorithm is to determine the matrix of the weights $\boldsymbol{w}_i$ and the vector of the bias values $\boldsymbol{b}_i$ that leads to a good approximation of the known outputs, i.e. $y_l^{(N)} \approx y_l, l = 1, \dots, p$. This goal can be obtained by minimizing a cost function $C : R^n \to R$, whose role is to quantify the performance of prediction capability of the ANN, such that

$$\boldsymbol{w}^{(i)}, \boldsymbol{b}^{(i)} = \underset{\boldsymbol{w},\boldsymbol{b}}{\operatorname{argmin}}\, C(y^N(\boldsymbol{x}, \boldsymbol{w}, \boldsymbol{b})). \tag{10}$$

The above-stated minimization problem can be solved by using optimization methods, typically based on the evaluation of the cost function's gradient. The minimization procedure can be done by adopting the so-called back-propagation algorithm, which evaluates the gradient of the cost function C with respect to the weights and the biases through the use of the chain rule,

$$\begin{aligned}
&\frac{dC}{dw_{jk}^{(i)}} = \frac{dC}{dy_j^{(i)}}\frac{dy_j^{(i)}}{dz_j^{(i)}}\frac{dz_j^{(i)}}{dw_{jk}^{(i)}} = \frac{dC}{dy_j^{(i)}}\sigma_i'(z_j^{(i)})y_k^{(i-1)}\\
&\frac{dC}{db_j^{(i)}} = \delta_j^{(i)}\\
&\delta_j^{(i)} = w_{kj}^{(i+1)}\delta_k^{(i+1)}\sigma_i'(z_j^{(i)})\\
&\delta_j^{(N)} = \frac{dC}{dy_j}\sigma_i'(z_j^{(N)})
\end{aligned} \tag{11}$$

It is worth mentioning that by adopting the logistic activation function, its derivative can be simply expressed as $d\sigma/dx = \sigma(1-\sigma)$. Finally, the weights and the biases are updated by using the standard gradient descent algorithm,

$$\Delta w_{kj}^{(i)} = -\eta\frac{dC}{dw_{jk}^{(i)}} = -\eta\delta_j^{(i)}y_k^{(i-1)},\ \Delta b_j^{(i)} = -\eta\frac{dC}{db_j^{(i)}} = -\eta\delta_j^i \tag{12}$$

where $\eta > 0$ is the learning rate. The above expressions provide the updated weights and biases ($w_{kj}^{(i+1)} \leftarrow w_{kj}^{(i)} + \Delta w_{kj}^{(i)}, b_j^{(i+1)} \leftarrow b_j^{(i)} + \Delta b_j^{(i)}$) leading to a reduction of the cost function C.

3.2. Adopted ANNs

In order to solve the above-stated inverse design problem, two ANNs with different complexities, whose architecture is depicted in Fig. 3, have been adopted. For both the two ANNs, the activation function σ is assumed to be the well-known $ReLU$ (rectified linear, $ReLU(z_i) = \max(0, z_i)$, [37,42]) for the layers $1, 2, \dots, N-1$, and the sigmoid activation function ($\sigma(z_i) = (1 - e^{z_i})^{-1}$) has been adopted only for the last (Nth) layer of the ANN [42]. In particular, the following ANNs have been developed by assuming $m = q = p = 72$:

- ANN (1) is characterized by $N = 2$ layers with $q = 72$ neurons each;
- ANN (2) is characterized by $N = 6$ layers with $q = 72$ neurons each.

The loss function quantifying the error of the ANN prediction (Fig. 4) is defined as

$$\ell = \text{mean}(\boldsymbol{L}), \text{ with } \boldsymbol{L} = (\ell_1, \ell_2, \dots \ell_j, \dots, \ell_{N_T}) \\ \text{and } \ell_j = \sum_{i=1}^{p} (\bar{\mu}_{ANN(i)} - \bar{\mu}_{FEM(i)})^2 \tag{13}$$

where N_T is the number of cases used for training the ANN, while p represents the number of angular positions at which the difference $\bar{\mu}_{ANN} - \bar{\mu}_{FEM}$ is evaluated in the elastic layer.

4. Design of swelling-induced shape change

In the present section, we illustrate the use of the ANN-based approach for the inverse design of a system that is capable of achieving a target shape in response to swelling-induced forces through two ANNs with different architectures.

4.1. ANN training

The training process is performed by assigning the vector of the final radius $r(\theta)$, corresponding to the target shape, discretized through the vector $r_h, (h = 1, \dots, m = 72)$, i.e. by specifying the radius value at steps of 5° over the 2π angle. The output vector is the shear modulus collected in the vector $\mu_h(\theta), (h = 1, \dots, p = 72)$.

To generate the data required for training, we define the dimensionless shear distribution values $\bar{\mu}_{rand}(\theta_j) = \mu_{rand}(\theta_j)/\mu_{max}$ with $j = 1, \dots, m = 72$. In the cases we consider, $\bar{\mu}_{rand}(\theta_j) \in [0.05, 1]$ and we set $\mu_{max} = 660\,\text{kPa}$, corresponding to a Young's modulus $E_{max} = 2$ MPa in incompressible materials.

The distribution of the dimensionless shear parameter values μ^*, whose values fall within the range $[-M, M]$, is randomly generated at discrete angle intervals over the 2π angle, through a combination of M sinusoidal functions via

$$\mu^*_{rand}(\theta_j) = \sum_{i=1}^{M} A_i \sin(B_i \theta_j + C_i). \tag{14}$$

Here, A_i is a randomly generated number with a uniform distribution in the interval $[0, 1]$, and B_i and C_i are randomly generated numbers with a uniform distribution in the interval $[1, n]$; the random parameter n, here assumed equal to 20, is related to the number of peaks of the function $\mu^*_{rand}(\theta_j)$ in the angular interval $[0, 2\pi]$. The number of terms is taken equal to $M = 4$.

Once a function $\mu^*_{rand}(\theta_j)$ is defined, the dimensionless shear modulus $\bar{\mu}$ is computed by linearly mapping it in the range of interest, which in this case is $0.05 \le \bar{\mu} \le 1$.

As for the gel, the fluid-network interaction parameter has been assumed to be equal to $\chi = 0.55$ (see Fig. 4).

Table 1
Errors e, calculated according to Eq. (16), quantifying the difference between the target shapes and the FEM results obtained by using the shear modulus provided by the ANNs 1, and 2 for the four considered target shapes A, B, C, and D shown in Fig. 5.

ANN	A	B	C	D
1	9.15×10^{-4}	1.05×10^{-4}	6.74×10^{-4}	2.75×10^{-4}
2	7.63×10^{-4}	1.02×10^{-4}	5.11×10^{-4}	3.22×10^{-4}

A total of $N_c = 1200$ cases have been prepared by randomly generating the shear modulus distribution according to the above procedure based on Eq. (14) and subsequently used in FE simulations (see Section 2.1) to obtain the final shape induced by swelling. Some examples of the FEM results based on randomly generated shear modulus distribution are shown in Fig. 2. The steady-state shapes of the considered mechanical system obtained by FEM simulations are then used to train the ANNs characterized by the architectures illustrated in Section 3.2. Among the FE simulated cases, $N_T = 1000$ have been used for training the ANNs and $N_V = 200$ have been used for the validation.

4.2. Inverse design of the stiffness distribution in the elastic layer

Next, the ANN is used to design the shear modulus distribution that achieves the required target shapes in a gel-elastic layer system. To this end, we employ the simple analytical expression of closed-shape geometries,

$$\begin{bmatrix} x_0(\theta) \\ y_0(\theta) \end{bmatrix} = (|\cos(n_v\theta/4)| + |\sin(n_v\theta/4)|)^c \begin{bmatrix} \cos\beta & -\sin\beta \\ \sin\beta & \cos\beta \end{bmatrix} \begin{bmatrix} S \cdot \cos\theta \\ \sin\theta \end{bmatrix}, \tag{15}$$

which allows us to define a wide range of shapes characterized by a different number of vertices, size, and orientation in the x–y plane [43]. In Eq. (15), n_v is the number of vertices of the closed shape, c is related to the convexity ($c > 0$) or concavity ($c < 0$) of the edges, β is the rotation of the whole closed shape in the x–y plane, $-\pi \le \theta \le \pi$, and S is a scaling factor.

Based on Eq. (15), we choose four target shapes which are illustrated in Fig. 5. The dimensionless shear modulus distributions in the elastic layer provided by the two ANNs for the four target shapes are depicted in Fig. 6 and the corresponding deformed shapes of the external line of the elastic layer – obtained by FEM simulations by using the shear modulus distributions provided by the two ANNs – are shown in Fig. 7.

We find that the stiffness distributions provided by the two ANNs are very similar and present peaks and valleys according to the number of vertexes of the desired shape (Fig. 5).

The corresponding deformed shapes obtained by FEM are also almost identical, irrespective of the ANN used (see Fig. 7). As expected, we find that stiffer regions lead to smaller deformations while softer areas in the tubular elastic layer experience larger displacements.

The undeformed and the deformed mesh of the FEM simulations performed by using the shear modulus provided by the ANN (2) together with the required target shapes, are shown in Fig. 8.

To quantify the difference between the ANN predictions and the FE results, for each case we define the error

$$e = \text{mean}(\boldsymbol{\mathcal{E}}), \text{ with } \boldsymbol{\mathcal{E}}^T = (e_1, \dots, e_i, \dots) \\ \text{and } e_i = (\bar{r}_{target(i)} - \bar{r}_{FEM(i)})^2, \; i = 1, 2, \dots, m \tag{16}$$

where $\bar{\bullet} = \bullet/r_0$ indicates the dimensionless radius and r_0 is the initial external radius of the elastic circular tube layer surrounding the unswollen gel. The errors, reported in Table 1, reveal that the two ANN networks provide sufficient accuracy of prediction, irrespective of the complexity of their architecture.

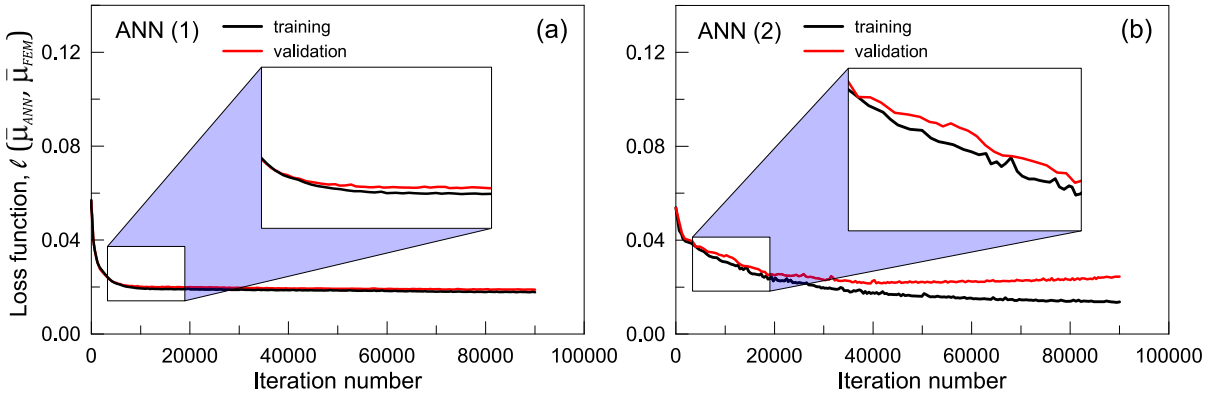

Fig. 4. Loss function for the training (done with 85% of the available data) and the validation (evaluated by using 15% of the available data) performed with the ANN (1) (a) and the ANN (2) (b).

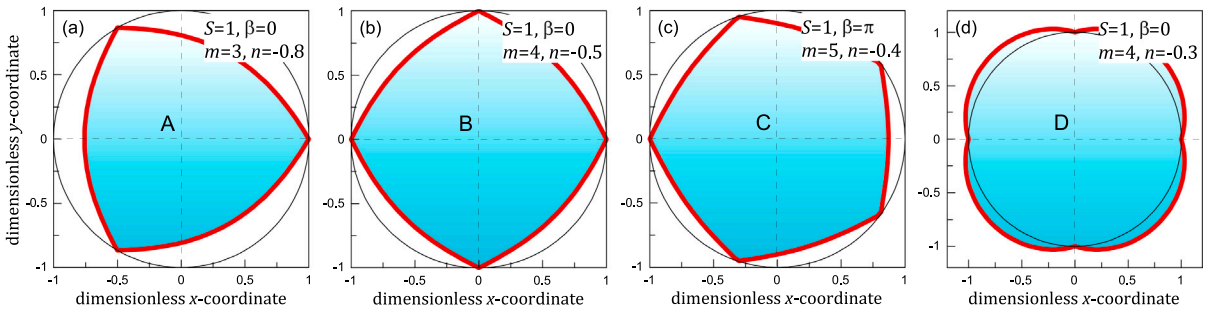

Fig. 5. Plot of the four target shapes (obtained by using the parametric expressions reported in Eq. (15) for some choices of the parameters n and m) used as input to the ANNs.

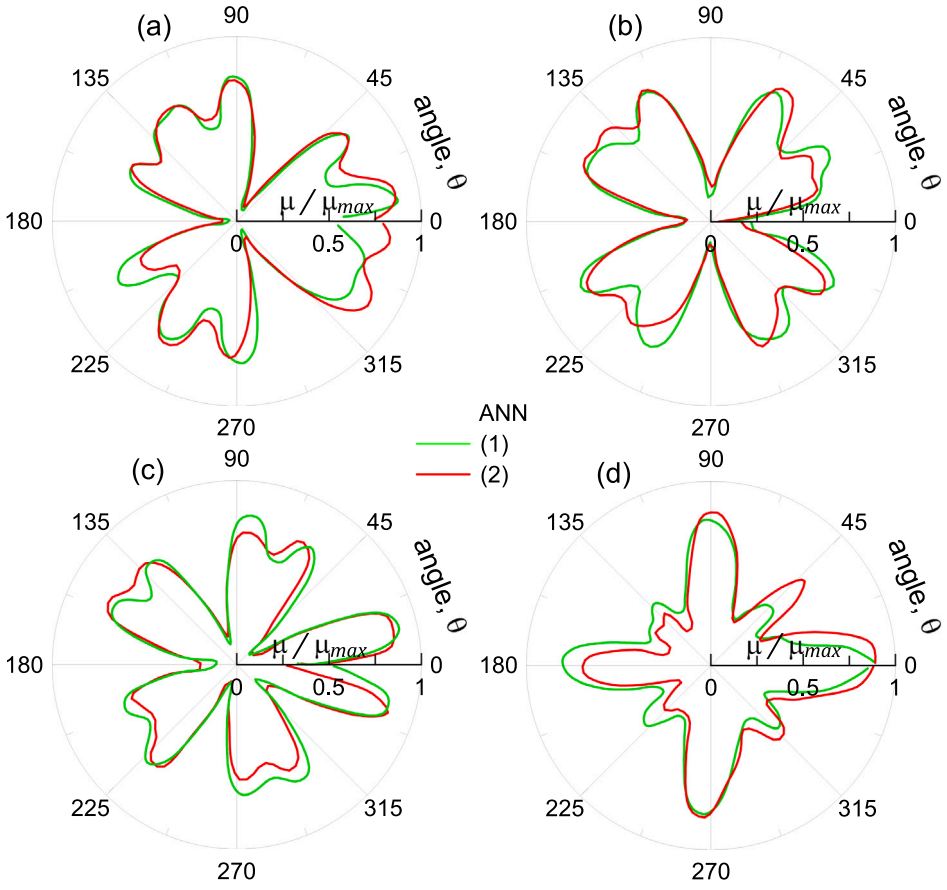

Fig. 6. Dimensionless shear modulus $\bar{\mu} = \mu/\mu_{max}$ distribution obtained by using the two ANNs (1, 2) according to the four target shapes A, B, C, and D shown in Fig. 5.

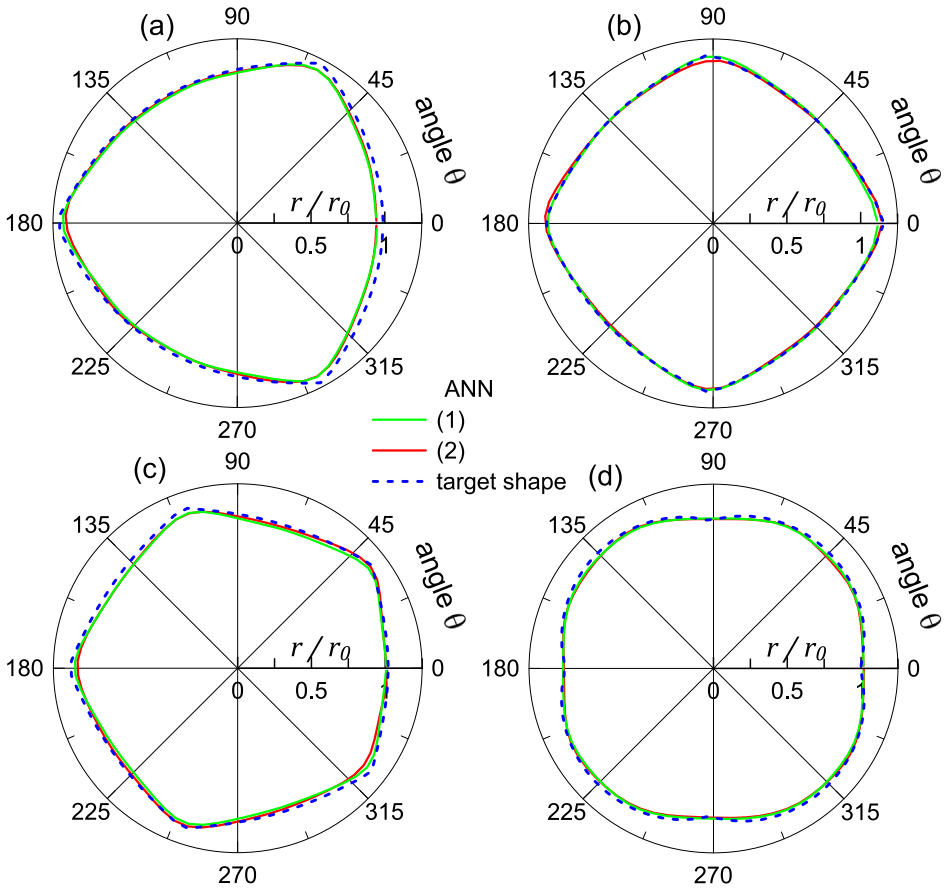

Fig. 7. Morphed shapes obtained by FEM simulations by using the shear modulus distributions provided by the two ANNs (1, 2, see Fig. 6) according to the four target shapes A, B, C, and D shown in Fig. 5.

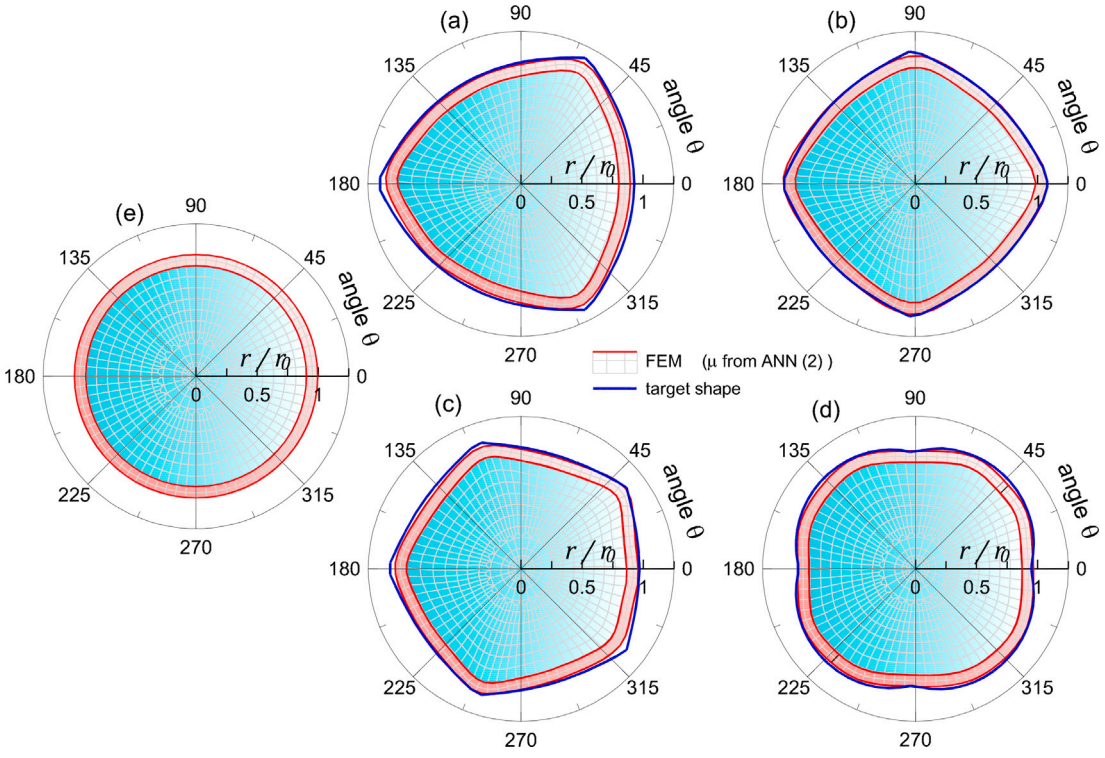

Fig. 8. Deformed FEM shapes obtained by using the shear modulus distributions provided by the ANN (2), see Fig. 6 related to the four target shapes (a, b, c, d) shown in Fig. 5. Undeformed mesh (e).

5. Conclusions

In this work, we have considered the problem of controlling the shape change in gel-driven systems where an elastic layer surrounds a gel core whose role is to produce pressure, induced by swelling, against the layer itself. Designing a proper stiffness distribution within the elastic layer enables obtaining different shapes that are precisely controllable. Through the use of a machine learning-based approach using an artificial neural network, we have shown that the gel-elastic layer system can produce quite different shapes whose geometry can be tuned at will. This strategy for obtaining shape change in swollen gel-driven systems is suitable to be used in a variety of applications such as soft grippers, small-scale hydraulic valves targeting specific channel cross-sections, etc. In vivo applications will also benefit from the use of hydrogels with shape change capabilities by harnessing their improved diagnostics and therapeutic characteristics [44]. This approach enables finding the required stiffness distribution to precisely mimic the desired shape upon swelling of the gel core. This approach to controlling the shape change in structures represents a new strategy for designing active structures.

The design space of this kind of system can become even wider if the swelling degree, i.e. the amount of fluid uptaken by the network, can be controlled by environmental stimuli such as temperature change, enabling a self-controllable shape change.

CRediT authorship contribution statement

Silvia Monchetti: Writing – review & editing, Software, Investigation. **Roberto Brighenti:** Writing – original draft, Supervision, Methodology, Conceptualization. **Tamara Hanuhov:** Writing – review & editing, Conceptualization. **Noy Cohen:** Writing – review & editing, Supervision, Formal analysis, Conceptualization.

Declaration of competing interest

The authors declare that they have no known competing financial interests or personal relationships that could have appeared to influence the work reported in this paper.

Data availability

Data will be made available on request.

Acknowledgments

The authors thank Prof. Aviv Tamar for helpful discussions.

References

[1] N. Chirani, L. Yahia, L. Gritsch, F.L. Motta, S. Chirani, S. Farè, et al., History and applications of hydrogels, J. Biomed. Sci. 4 (02) (2015) 1–23.
[2] J.F. Louf, N.B. Lu, M.G. OConnell, H.J. Cho, S.S. Datta, Under pressure hydrogel swelling in a granular medium, Sci. Adv. 7 (7) (2021) eabd2711.
[3] A. Parodi, S.M. Khaled, I.K. Yazdi, M. Evangelopoulos, N.E.T. Furman, X. Wang, F. Urzi, S. Hmaidan, K.A. Hartman, E. Tasciotti, Smart hydrogels, in: B. Bhushan (Ed.), Encyclopedia of Nanotechnology, Springer Netherlands, Dordrecht, 2016, pp. 3735–3747.
[4] A.S. Hoffman, Stimuli-responsive polymers: Biomedical applications and challenges for clinical translation, Adv. Drug Deliv. Rev. 65 (1) (2013) 10–16.
[5] A. Plummer, C. Adkins, J.-F. Louf, A. Košmrlj, S.S. Datta, Obstructed swelling and fracture of hydrogels, Soft Matter 20 (7) (2024) 1425–1437.
[6] V. Zamani, T.J. Pence, H. Demirkoparan, H. Topol, Hyperelastic models for the swelling of soft material plugs in confined spaces, Int. J. Non-Linear Mech. 106 (2018) 297–309.
[7] R. Brighenti, M.P. Cosma, Swelling mechanism in smart polymers responsive to mechano-chemical stimuli, J. Mech. Phys. Solids 143 (2020) 104011.
[8] R. Brighenti, M.P. Cosma, Mechanics of multi-stimuli temperature-responsive hydrogels, J. Mech. Phys. Solids 169 (2022) 105045.
[9] I. Khmelinskii, V.I. Makarov, On the effects of mechanical stress of biological membranes in modeling of swelling dynamics of biological systems, Sci. Rep. 10 (1) (2020) 8395.
[10] R. Brighenti, M.P. Cosma, N. Cohen, Mechanics and physics of the light-driven response of hydrogels, Mech. Res. Commun. 129 (2023) 104077.
[11] N. Cohen, Programming the equilibrium swelling response of heterogeneous polymeric gels, Int. J. Solids Struct. 178 (2019) 81–90.
[12] A.H. Velders, J.A. Dijksman, V. Saggiomo, Hydrogel actuators as responsive instruments for cheap open technology (HARICOT), Appl. Mater. Today 9 (2017) 271–275.
[13] X. Liu, S. Tian, F. Tao, W. Yu, A review of artificial neural networks in the constitutive modeling of composite materials, Composites B 224 (2021) 109152.
[14] N. Ravi, A. Mitra, P. Hamilton, F. Horkay, Characterization of the network properties of poly (ethylene glycol)–acrylate hydrogels prepared by variations in the ethanol–water solvent composition during crosslinking copolymerization, J. Polym. Sci. B: Polym. Phys. 40 (23) (2002) 2677–2684.
[15] M. Levin, N. Cohen, Swelling under constraints: Exploiting 3D-printing to optimize the performance of gel-based devices, Adv. Mater. Technol. 8 (14) (2023) 2202136.
[16] R. Brighenti, F. Artoni, F. Vernerey, M. Torelli, A. Pedrini, I. Domenichelli, E. Dalcanale, Mechanics of responsive polymers via conformationally switchable molecules, J. Mech. Phys. Solids 113 (2018) 65–81.
[17] T. Hanuhov, R. Brighenti, N. Cohen, Energy harvesting with dielectric elastomer tubes: active and (responsive materials-based) passive approaches, Smart Mater. Struct. 33 (5) (2024) 055004.
[18] P. Du, F.-F. Wang, J. Wang, On a simplified multi-layered plate model of growth: Asymptotic analyses and numerical implementation, Thin-Walled Struct. 191 (2023) 111100.
[19] Y. Kim, J. van den Berg, A.J. Crosby, Autonomous snapping and jumping polymer gels, Nature Mater. (2021) 1–7.
[20] Y. Lee, W. Song, J.-Y. Sun, Hydrogel soft robotics, Mater. Today Phys. 15 (2020) 100258.
[21] Z. Shen, F. Chen, X. Zhu, K.-T. Yong, G. Gu, Stimuli-responsive functional materials for soft robotics, J. Mater. Chem. B 8 (39) (2020) 8972–8991.
[22] S. Zu, Z. Wang, S. Zhang, Y. Guo, C. Chen, Q. Zhang, T. Liu, Q. Liu, Z. Zhang, A bioinspired 4D printed hydrogel capsule for smart controlled drug release, Mater. Today Chem. 24 (2022) 100789.
[23] A. Herrmann, R. Haag, U. Schedler, Hydrogels and their role in biosensing applications, Adv. Healthc. Mater. 10 (11) (2021) 2100062.
[24] Z.U. Arif, M.Y. Khalid, A. Tariq, M. Hossain, R. Umer, 3D printing of stimuli-responsive hydrogel materials: Literature review and emerging applications, Giant (2023) 100209.
[25] J. Karvinen, M. Kellomäki, Characterization of self-healing hydrogels for biomedical applications, Eur. Polym. J. (2022) 111641.
[26] W. Sun, A.S. Williamson, R. Sukhnandan, C. Majidi, L. Yao, A.W. Feinberg, V.A. Webster-Wood, Biodegradable, sustainable hydrogel actuators with shape and stiffness morphing capabilities via embedded 3D printing, Adv. Funct. Mater. (2023) 2303659.
[27] K. Zhang, Y. Zhou, J. Zhang, Q. Liu, C. Hanenberg, A. Mourran, X. Wang, X. Gao, Y. Cao, A. Herrmann, et al., Shape morphing of hydrogels by harnessing enzyme enabled mechanoresponse, Nature Commun. 15 (1) (2024) 249.
[28] P.J. Yang, A.B. Lee, M. Chan, M. Kowalski, K. Qiu, C. Waid, G. Cervantes, B. Magondu, M. Biagioni, L. Vogelnest, et al., Intestines of non-uniform stiffness mold the corners of wombat feces, Soft Matter 17 (3) (2021) 475–488.
[29] W. Hong, X. Zhao, J. Zhou, Z. Suo, A theory of coupled diffusion and large deformation in polymeric gels, J. Mech. Phys. Solids 56 (5) (2008) 1779–1793.
[30] S.A. Chester, L. Anand, A coupled theory of fluid permeation and large deformations for elastomeric materials, J. Mech. Phys. Solids 58 (11) (2010) 1879–1906.
[31] N. Cohen, R.M. McMeeking, On the swelling induced microstructural evolution of polymer networks in gels, J. Mech. Phys. Solids 125 (2019) 666–680.
[32] T.J. Pence, On the formulation of boundary value problems with the incompressible constituents constraint in finite deformation poroelasticity, Math. Methods Appl. Sci. 35 (15) (2012) 1756–1783.
[33] M.L. Huggins, Thermodynamic properties of solutions of long-chain compounds, Ann. New York Acad. Sci. 43 (1) (1942) 1–32.
[34] P.J. Flory, Thermodynamics of high polymer solutions, J. Chem. Phys. 10 (1) (1942) 51–61.
[35] R. Brighenti, M.P. Cosma, Swelling mechanism in smart polymers responsive to mechano-chemical stimuli, J. Mech. Phys. Solids 143 (2020) 104011.
[36] T. Tanaka, D.J. Fillmore, Kinetics of swelling of gels, J. Chem. Phys. 70 (3) (1979) 1214–1218.
[37] S. Chakraverty, S.K. Jeswal, Applied Artificial Neural Network Methods for Engineers and Scientists: Solving Algebraic Equations, World Scientific, 2021.
[38] S. Xiao, J. Li, S.P.A. Bordas, T.Y. Kim, Artificial neural networks and their applications in computational materials science: A review and a case study, Adv. Appl. Mech. (2023) 1–33.

[39] L.G. Wright, T. Onodera, M.M. Stein, T. Wang, D.T. Schachter, Z. Hu, P.L. McMahon, Deep physical neural networks trained with backpropagation, Nature 601 (7894) (2022) 549–555.
[40] C. Anitescu, B. İsmail Ateş, T. Rabczuk, Physics-informed neural networks: Theory and applications, in: Machine Learning in Modeling and Simulation: Methods and Applications, Springer, 2023, pp. 179–218.
[41] J. Bai, T. Rabczuk, A. Gupta, L. Alzubaidi, Y. Gu, A physics-informed neural network technique based on a modified loss function for computational 2D and 3D solid mechanics, Comput. Mech. 71 (3) (2023) 543–562.
[42] S.R. Dubey, S.K. Singh, B.B. Chaudhuri, Activation functions in deep learning: A comprehensive survey and benchmark, Neurocomputing 503 (2022) 92–108.
[43] A. Mirabolghasemi, A. Akbarzadeh, D. Rodrigue, D. Therriault, Thermal conductivity of architected cellular metamaterials, Acta Mater. 174 (2019) 61–80.
[44] G. Chakrapani, M. Zare, S. Ramakrishna, Intelligent hydrogels and their biomedical applications, Mater. Adv. (2022).